

Calibration and testing of the ST7 capacitive sensor using an optical interferometer with fiber optic input and output

This article has been downloaded from IOPscience. Please scroll down to see the full text article.

2006 J. Phys.: Conf. Ser. 32 117

(<http://iopscience.iop.org/1742-6596/32/1/019>)

View [the table of contents for this issue](#), or go to the [journal homepage](#) for more

Download details:

IP Address: 38.107.179.210

The article was downloaded on 15/02/2012 at 03:28

Please note that [terms and conditions apply](#).

Calibration and testing of the ST7 capacitive sensor using an optical interferometer with fiber optic input and output

G. Allen, W. Bencze, R. Byer, A. Dang, D. Lauben, S. Dorlybounxou, J. Hanson, S. Higuchi, L. Ho, G. Huffman, F. Sabur, K. Sun, R. Tavernetti, L. Rolih, R. VanPatten, J. Wallace, S. Williams

Hanson Experimental Physics Laboratory, Stanford University, Stanford, CA 94305-4085, USA
E-mail: gsallen@stanford.edu

Abstract. We describe the calibration and operation of the ST7 GRS capacitive sensor system. A novel optical interferometer, featuring both fiber optic delivery and readout, is used for calibration of the capacitive sensor system and as a witness sensor during testing. The capacitive sensor showed $1 \text{ nm}/\sqrt{\text{Hz}}$ performance from 1 mHz to 10 Hz. Above 10 mHz the optical system showed significantly better performance than the capacitive sensor, with a noise floor at $2 \times 10^{-11} \text{ m}/\sqrt{\text{Hz}}$ and a longer measurement standoff distance. The optical system was limited to $5 \text{ nm}/\sqrt{\text{Hz}}$ at 1 mHz due to thermal disturbances of the laboratory environment, and could be reduced with a revised design and/or improved thermal stability.

1. Introduction

The ST7 mission was designed as a validation mission to show that the currently proposed LISA design of cubical proof-mass can achieve the performance required for the LISA mission. The idea behind ST7 was to show that a satellite with two proof-masses can maintain drag-free operation along a single axis with acceleration noise of less than $3 \times 10^{-14} \text{ m}/(\text{s}^2\sqrt{\text{Hz}})$ at 1 mHz. The acceleration noise arises from two sources, the first is direct forces on the proof mass, and the second is the stiffness coupling between the proof-mass and the spacecraft. This performance is similar to that required for LISA, and represents a significant challenge in spacecraft design. ST7 would have shared a spacecraft with the similar European Space Agency LTP (LISA Technology Package) mission. Both LTP and ST7 will test candidate technologies for use in LISA [1].

At the core of the satellite is the gravitational reference sensor (GRS), which consists of a proof-mass, housing, and the sensing and forcing systems. The proof-mass is a 4-cm cube made of a gold/platinum alloy for high-density and a near-zero magnetic susceptibility. The housing contains the electrodes that are used for the capacitive sensing system, and for electrostatic forcing. The capacitive sensing system is required to meet $3 \text{ nm}/\sqrt{\text{Hz}}$ in the LISA bandwidth (1 mHz - 1 Hz) to provide adequate signal for the drag-free control algorithm.

The main gravitational wave signal for LISA will be detected by an interferometric link between the satellites. To verify the residual proof mass acceleration the ST7 mission uses an interferometric link to measure the displacement between the proof-masses and the satellite.

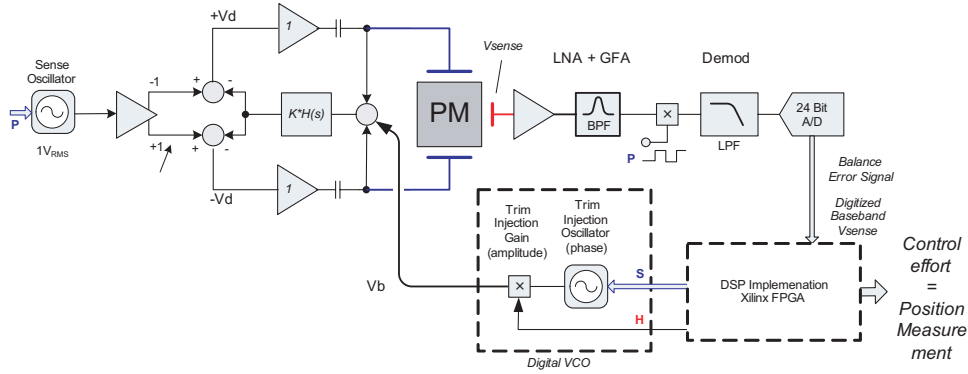


Figure 1. ST7 Capacitive sensor block diagram for one channel. The drive, trim and demodulation electronics are separate for each channel.

Each proof-mass is measured with a separate interferometer, and the residual acceleration is the difference of the two measurements.

2. ST7 Capacitive Sensor

The capacitive sensor housing and proof mass form the core of the ST7 GRS. The basic electrode configuration is 1-4-2 electrodes per face (X-Y-Z), where X is the sensitive measurement axis requiring the most stringent resolution and orientation control. Angles are computed by taking the difference of electrodes on the same face, while position is the sum.

The basic measurement technique is a three-arm bridge measurement, where opposite polarity sine waves are applied to opposing electrodes, and the residual voltage on the proof-mass (PM) is observed by a pick-up electrode (Figure 1) [2]. The drive sine wave (V_d) is generated by a low-pass filtered, pulse-width modulated tri-state signal ($+V, 0, -V$), generated by a digital signal processing chip (Xilinx FPGA). Using the FPGA for sine wave generation guarantees phase stability between the sine wave and the square-wave demodulation signal. The cancellation of the sine waves keeps the proof-mass at a virtual ground. The residual voltage on the proof-mass is sensed with four low-noise amplifiers (LNAs) attached to pick-up electrodes on the Y & Z faces. To avoid direct coupling of drive to the pick-up electrode, only pick-up electrodes on orthogonal faces from the drive electrodes are used (ie, Y-axis measurements use Z face pick-ups). The LNA signal is passed to a high-gain amplifier, where the signal is amplified further and summed with the other LNA signals for that face. The signal is then demodulated using a square wave demodulator. A trim balance signal (V_b) is injected along with the drive to null the return signal for any proof-mass location. The sensor can operate in "auto-balance" mode, where the trim signal is continuously adjusted by the FPGA above the science band (to 1 kHz) for reduced spacecraft to proof-mass stiffness coupling. The current design uses auto-balance as a baseline for the stiffness reduction, but can also be operated with one-time fixed trim if auto-balance is observed to introduce excess noise.

The expected sensitivity for a single channel can be calculated using a parallel plate model for capacitance. The expected capacitance between an electrode face and the proof-mass as a function of x , the displacement from the housing center, can be written as,

$$C(x) = \epsilon_0 \frac{A}{d \pm x} \approx C_0 \left(1 \mp \frac{x}{d} \right), \quad (1)$$

where $C_0 = \frac{\epsilon_0 A}{d}$ is the nominal capacitance between the electrode and the proof mass, d is the nominal gap size. Given a simple bridge circuit, with pickup electrode, the voltage on the test

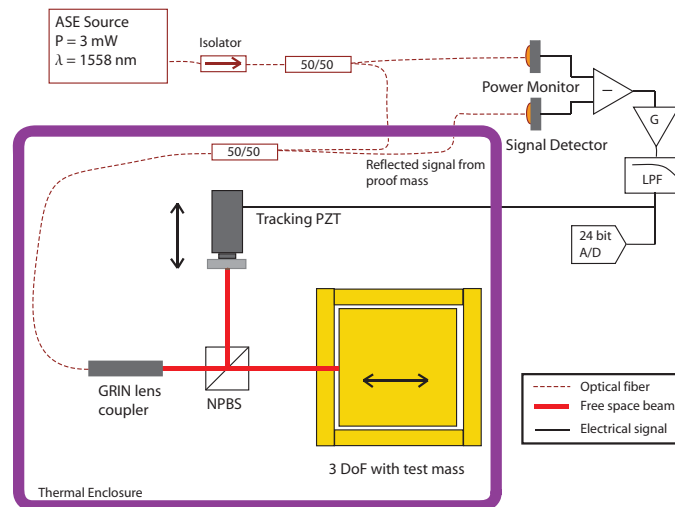


Figure 2. Optical interferometer designed for use with the ST7 GRS. The short coherence length of the source requires that the arm lengths are matched. The control effort used to keep the interferometer locked is used as a position measurement. The piezo-electric transducer is the only active component in the thermal chamber.

mass (V_{tm}) is given by

$$V_{tm} = \sum_i \frac{C_i V_i}{\Sigma C} \approx 2 \frac{C_0}{\Sigma C} \frac{x}{d} V_d \quad . \quad (2)$$

This voltage is then sensed by a LNA attached to a sense electrode. The read-out signal is then demodulated to base-band and digitized for use by the flight computer. The drive voltage is designed with part per million relative stability, leading to the LNA as the limiting noise source with $V_n = 35 \text{ nV}/\sqrt{\text{Hz}}$ voltage noise referred to the proof-mass. The capacitive sensor resolution is therefore constrained by the read-out noise from the low-noise amplifier and the maximum allowable drive voltage, which is limited by stiffness constraints [3].

3. Optical Read-out

For initial calibration and diagnostic purposes, the 3-DoF test fixture is also equipped with an optical interferometer (Figure 2). The interferometer is a tracking Michelson interferometer similar to the one described by Gray, et al [4]. The main difference is that the light is delivered by an optical fiber with a GRIN lens collimator, and the read-out signal is retro-reflected back into the optical fiber. The fiber feed and read-out allows the source and detector electronics to be located off the optical bench. The only active component on the optical bench is the feedback PZT, which dissipates very little heat. Mounting constraints for the optical sensor required using required arm lengths of approximately 4 cm, which is roughly 20 times more sensitive length than the capacitive sensor.

The light source is an unpolarized $1.55 \mu\text{m}$ Amplified Spontaneous Emission source, with a coherence length of approximately $100 \mu\text{m}$. The light is delivered via standard SMF-28 fiber to the 3-DoF chamber, and delivered via a GRIN lens collimator. The return signal from the Michelson interferometer is re-collimated and a 50/50 splitter is used as a circulator to divert this light to a detector. The current design back-couples about 25% of the return signal, due to the large working distance of the GRIN lens. Back-coupled efficiency of greater than 95% is

possible with either shorter path length or a re-optimized collimation system. The substantial loss of the return signal is unimportant for ground testing because the 4 mW of supplied power is more than sufficient to get above the detector noise floor.

The interferometer was designed to be a simple, robust and compact to match the performance of the capacitive sensor system. We also tested an interferometer configuration with optical fiber in the sensitive path, leading to a much shorter working distance and excellent return coupling. Each arm of the interferometer had roughly 50 cm of optical fiber, laid in parallel, in the path. This configuration provided excellent cancellation of thermal drift, but stress effects in the fiber significantly degraded performance. The fiber in path configuration showed sudden jumps of up to $\pi/20$ in the optical phase, leading to a noise floor that was roughly 20 times worse than the free-space configuration. These jumps are probably caused by stress induced index of refraction changes in the optical fiber, and are possibly associated with the specific choice of the external cladding of the optical fiber. The main implication of this testing is that any time optical fiber is used in a phase sensitive path, such as the fiber link between the LISA proof-masses, the system should be carefully tested to ensure that there is good common mode cancellation of possible disturbances.

The control loop uses slope locking at the mid-fringe point to lock the interferometer phase to the input intensity. This provides approximately 20 dB of cancellation of intensity noise. The position signal is proportional to the control effort required to maintain the interferometer at the mid-fringe point. Using a tracking arrangement allows the interferometer to operate over 10 μm without the need for fringe counting. The peak of the coherence envelope provides an effective zero position of approximately 2 μm , when the interferometer arm lengths are matched. This provides the optical system with a degree of absolute distance measurement. The limiting noise source for the interferometer is the mechanical stability of the interferometer mounting apparatus. At low frequency this is dominated by thermal expansion of the mounting stages. This limited the low-frequency performance of the interferometer, however the interferometer was a very valuable tool for diagnostic and for calibration purposes.

We are also concerned with the absolute accuracy of the interferometer, since it is used to calibrate the capacitive sensor during testing. The error associated with the center wavelength is small, the measured shift in the center wavelength was less than 5 nm over the entire range of output power. The control loop has a closed-loop, round-trip loop gain of approximately 700, therefore the DC tracking error is small. The voltage to position scale factor of the PZT is measured by sweeping the PZT across an interferometer fringe, and can be measured to 1%. The dominant error term is creep in the PZT, which we observed to be about 8% of the step motion. Hysteresis in the PZT, is typically 10%, but we can expect lower hysteresis in practice. This is because the cube is moved several consecutive steps in the same direction, and only the measurement from the last step is used. A more thorough study of open-loop piezoelectric actuators by Jung, et al. found that the total error for 1 μm step motions to be roughly 50 nm, which is consistent with the creep motion shown in Figure 3 [5]. Based on these errors sources, we consider conservative estimate of 10% accuracy on the calibration to be reasonable.

4. Optical and capacitive cross correlation procedure and results

For electronics testing of the capacitive sensor, a GRS housing capable of actuating a proof-mass in three degrees-of-freedom (3-DoF) was built to closely simulate the behavior of the GRS. The proof-mass is a 4 cm cube made of stainless steel, with one face polished for use with the interferometer, supported by three registration points on the bottom face. For comparison, the flight proof-mass would be made of a Gold/Platinum alloy with a gold coating. Prototype housing walls were used for the capacitive sensing system. The housing proof-mass mount allowed for linear motion in two axes (Y,Z) and rotation around the X-axis.

Starting from a squared and centered orientation, the amplified capacitive sensor signal is viewed

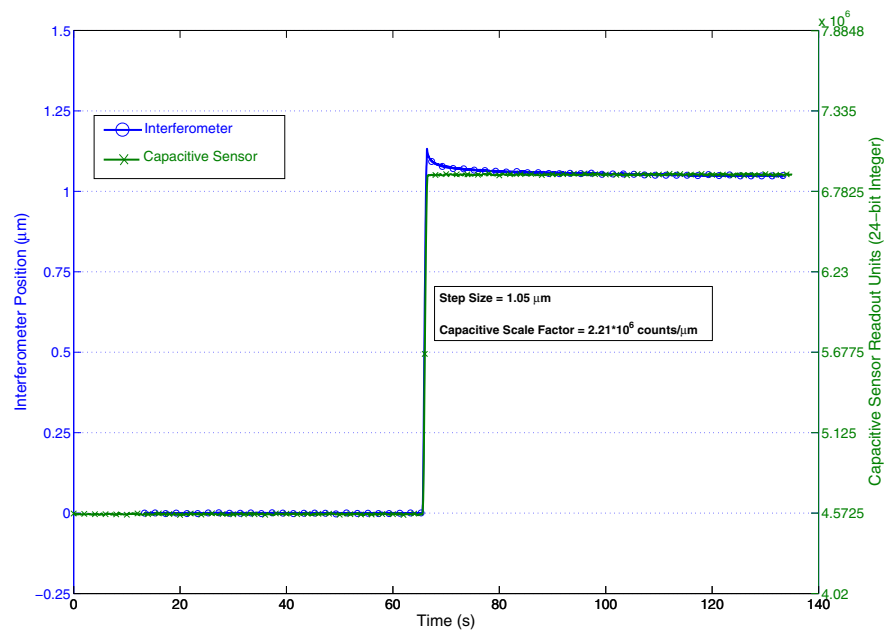


Figure 3. A typical calibration step. The commanded motion was $1.2 \mu\text{m}$, while the observed motion was $1.05 \mu\text{m}$. The settling time of the interferometer is due to creep in the piezo-electric actuator, which limits the absolute accuracy to 10%. The step size is determined by short segments of data taken 30 sec before and after the step.

on an oscilloscope. The cube is moved to minimize the amplitude of the return signal, indicating the electrical null. When the electrical null is found the return signal is then used to set the phase for the demodulator. The phase is set via a register in the FPGA, and is currently set by comparing the waveforms on an oscilloscope. For flight, the demodulator phase will be set by software, as part of the automatic initialization procedure.

Final alignment of the optical system is then done to verify that the optical system is working properly. The thermal chambers are closed, and the thermal stabilization system is activated. Once the demodulator phase is set, the demodulated signal is checked to make sure that it is nearly centered.

Figure 3 shows a typical calibration step. For calibration, the motor driven screws are used to move the proof-mass in $1 \mu\text{m}$ steps that are simultaneously observed by the capacitive sensor and the optical system. Each step is taken slowly enough to ensure that the interferometer control loop remains locked. For calibration, the position was chosen as the average of approximately 8 seconds of data taken roughly 30 seconds before and after the step. The motion as observed by the interferometer is then used to calculate a displacement scale factor for the capacitive sensor data, converting raw A/D units into meters. A typical calibration profile is shown in Figure 3. The system is then set to collect data for roughly 36 hours, giving time for the thermal environment to stabilize. This leaves the capacitive sensor operating typically within $5 \mu\text{m}$ of the initial capacitive null.

Figure 4 shows a comparison of capacitive sensor and interferometer data taken simultaneously, showing a striking difference in the relative performance. The capacitive system shows excellent stability, and is less sensitive to thermal fluctuations but has a higher noise floor. Above 10

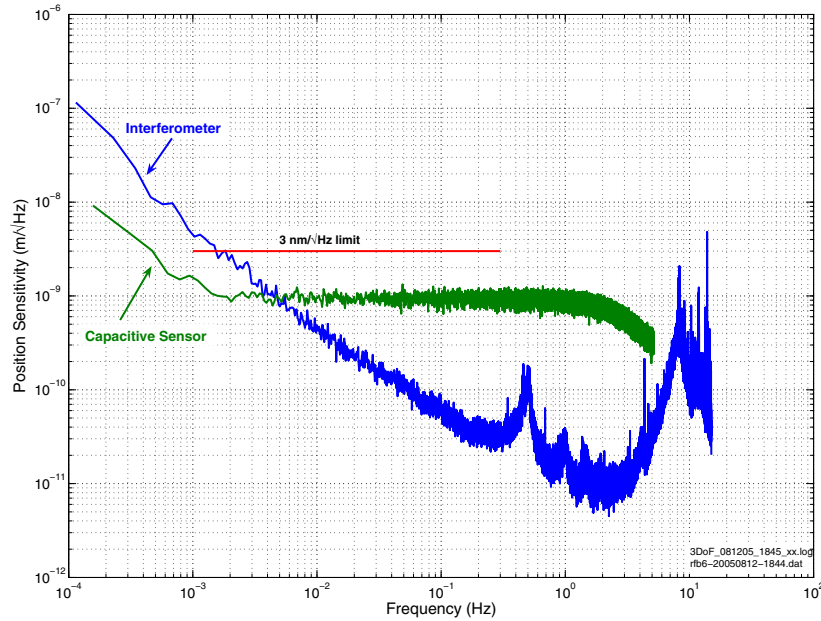


Figure 4. Capacitive and optical sensor noise floors observed during testing. The optical sensor’s low frequency performance is limited by the thermal stability of the optical mounts. The small peak at 0.5 Hz is a caused by the thermal stabilization system, and the peak at 8 Hz is a mechanical resonance in the mounting system.

mHz, the interferometer performance significantly exceeds the capacitive sensor. The peak at roughly 15 Hz is due to the mechanical resonance of the mounts used for the interferometer. At low frequencies, the interferometer performance is degraded by the thermal sensitivity of the mounting hardware. Thermal testing of the 3-DoF showed that the interferometer has a temperature coefficient of 6×10^{-6} m/K, and the capacitive sensor coefficient is 1×10^{-6} m/K. The thermal chamber stabilization system is able to reduce thermal noise to $1 \text{ mK}/\sqrt{\text{Hz}}$ at 1 mHz, but this still makes thermal drift a dominant error source at low frequencies (<10 mHz). The higher thermal sensitivity of the optical system is due to the use of steel and aluminum to construct the optical mounts, combined with a measurement baseline that is 20 times larger than the capacitive sensor. The performance of the optical system could be significantly improved by eliminating excess path length, so that the sensitive path length is purely the proof-mass to housing gap, and moving to optical mounts with a much lower thermal expansion coefficient, such as the main interferometer for ST7 [6].

For the test shown here, a $1.5 V_{\text{rms}}$ sine-wave was applied to a single 1/4-face electrode pair, and read-out with a single LNA. Additionally, a second 1/4-face electrode pair was also active with an equal amplitude sine wave, to look for possible cross-couplings between channels. This represents a worst-case scenario as the sensitive X-axis has over four times the drive area and takes advantage of all 4 LNAs, which allows the drive voltage to be reduced to $0.2 V_{\text{rms}}$ for lower electrostatic stiffness. This provides a comfortable margin on the performance requirement of $3 \text{ nm}/\sqrt{\text{Hz}}$. For a full description of the ST7 capacitive sensor testing, the reader should refer to Lauben et. al [2].

5. Conclusion

Calibration and testing of the ST7 GRS was significantly enhanced by the use of an external optical interferometer. The optical interferometer provides a calibration scale factor for the capacitive sensor. The capacitive sensor then measures the proof-mass displacement with a noise level $1 \text{ nm}/\sqrt{\text{Hz}}$ at 1 mHz. The optical sensor showed significantly better performance than the capacitive sensor above 10 mHz, at the expense of a dynamic range of $10 \mu\text{m}$. The low frequency performance of the system was limited by the thermal stability of the optical components. Extending this design to LISA would require the use of a ULE optical bench to make the thermally-related motion negligible, resulting in a design similar to the ST7 interferometer. A novel feature of this design is that the detectors are fiber coupled and not located on the optical bench. This sacrifices optical power, but improves the thermal environment by moving the detectors away from the sensitive components.

The optical sensor presented here shows performance very similar to that of two other optical sensors proposed to supplement the capacitive sensor system used on LISA or LTP. Acernese, et al. demonstrated a non-interferometric optical sensor with a noise floor $6 \text{ nm}/\sqrt{\text{Hz}}$ at 1 mHz, and a theoretical noise floor of $3 \times 10^{-10} \text{ m}/\sqrt{\text{Hz}}$ [7]. Speake and Aston have developed a compact interferometer with performance of $3 \times 10^{-12} \text{ m}/\sqrt{\text{Hz}}$ above 60 Hz, but did not show results in the LISA frequency band [8]. Our interferometer showed performance of $5 \text{ nm}/\sqrt{\text{Hz}}$ at 1 mHz, and a noise floor of $2 \times 10^{-11} \text{ m}/\sqrt{\text{Hz}}$ at 1 Hz. Additionally, by using the optical fiber for read-out, we eliminate the need to place any optical detectors on the GRS housing, reducing heat dissipation and simplifying mechanical design. The main interferometers for both ST7 and LTP are designed for higher performance, having to measure $1 \times 10^{-11} \text{ m}/\sqrt{\text{Hz}}$ at 3 mHz [9]. Our interferometer approaches this level of performance at 1 Hz, where the thermal noise is much less significant.

Based on our experiences developing and testing the GRS for ST7, we have proposed a modular GRS design for future missions, incorporating fiber optic delivery and read-out as a basis for optical sensing. The core of the modular design is a thin double-sided diffraction grating that serves as reference surface for both the proof-mass to spacecraft and the spacecraft to spacecraft measurements [10].

The interferometer is an invaluable tool for performance characterization of the capacitive sensor, by providing an independent, non-evasive, read-out of the relative proof-mass position. As LISA looks to include optical sensing to improve the GRS design, capacitive sensing will still be required for rough positioning and alignment. The results shown here demonstrate a mature capacitive sensor design, and show that optical sensing can provide significantly better resolution.

Acknowledgments

This research described in this paper was funded in part by the Jet Propulsion Laboratory under contracts 1252871, High-Precision Low-Cost Optical Readout System for Space-Borne Gravitational Reference Sensors and 1232133, Disturbance Reduction System: Gravitational Reference Sensor.

References

- [1] R Dolesi, D Bortoluzzi, P Bosetti, L Carbone, A Cavalleri, I Cristofolini, M DaLio, G Fontana, V Fontanari, B Foulon, C D Hoyle, M Hueller, F Nappo, P Sarra, D N A Shaul, T Sumner, W J Weber, and S Vitale. Gravitational sensor for lisa and its technology demonstration mission. *Classical and Quantum Gravity*, 20(10):S99–S108, 2003.
- [2] David Lauben et al. Electrostatic sensing and forcing electronics for the lisa pathfinder gravitational reference sensor, in preparation.
- [3] Bonny L Schumaker. Disturbance reduction requirements for LISA. *Classical and Quantum Gravity*, 20(10):S239–S253, 2003.
- [4] Malcolm B. Gray, David E. McClelland, Mark Barton, and Seiji Kawamura. A simple high-sensitivity

- interferometric position sensor for test mass control on an advanced LIGO interferometer. *Optical and Quantum Electronics*, 31(5-7):571–582, 1999.
- [5] Hewon Jung, Jong Youp Shim, and DaeGab Gweon. Tracking control of piezoelectric actuators. *Nanotechnology*, 12(1):14–20, 2001.
 - [6] Robert Spero and Andreas Kuhnert. The ST7 interferometer. *Classical and Quantum Gravity*, 21(5):S589–S595, 2004.
 - [7] F Acernese, E Calloni, R De Rosa, L Di Fiore, and L Milano. An optical readout system for the drag-free control of LISA. *Classical and Quantum Gravity*, 22(10):S279–S285, 2005.
 - [8] C C Speake and S M Aston. An interferometric sensor for satellite drag-free control. *Class. Quantum Grav.*, 22:S269, 2005.
 - [9] G Heinzl, V Wand, A García, O Jennrich, C Braxmaier, D Robertson, K Middleton, D Hoyland, A Rüdiger, R Schilling, U Johann, and K Danzmann. The ltp interferometer and phasemeter. *Classical and Quantum Gravity*, 21(5):S581–S587, 2004.
 - [10] Ke-Xun Sun, Graham Allen, Sasha Buchman, Dan DeBra, and Robert Byer. Advanced gravitational reference sensor for high precision space interferometers. *Classical and Quantum Gravity*, 22(10):S287–S296, 2005.